ACS OMEGA

Open Access

http://pubs.acs.org/journal/acsodf

Article

Glass-Bonded Monazite Waste Forms for Lanthanide and Actinide Immobilization: From Theoretical Design to Scale-Up Production and Characterization

Miroslava Peterson, Brian J. Riley,* Xiaonan Lu, Kayla H. Yano, Semanti Mukhopadhyay, Ian I. Leavy, Ethan K. Nickerson, Robert J. Seffens, Jincheng Du, Kyle D. Miller, and James E. Saal

Cite This: *ACS Omega* 2025, 10, 33524−33535

Read Online

ACCESS | Metrics & More | Article Recommendations | Supporting Information

ABSTRACT: The development of nuclear waste forms for both existing and future nuclear wastes is critical to ensuring global environmental safety. This study focuses on waste management from molten salt reactors, where fuel exists in a salt form and could be processed in real time for the removal of neutron poisons such as xenon isotopes (e.g., ^{135}Xe) and rare earth elements (REEs, e.g., ^{149}Sm). To ensure safe, stable, and long-term disposal in geological repositories, REEs must be incorporated into a durable waste form. Iron-phosphate glasses are a promising candidate due to their low melting points, high chemical durability, and their ability to incorporate high concentrations of REEs. In this study, we successfully prepared iron-phosphate glass waste forms with high Nd loadings (up to 37 mass %) in batch sizes ranging from small (23 g) to large (1600 g). The resulting materials contained up to 75 mass % $NdPO_4$, contributing to their mechanical resilience and exceptional chemical durability. These findings highlight the potential of iron-phosphate glasses as high-efficiency, chemically durable waste forms and demonstrate the successful transition from theoretical design to scaled-up production.

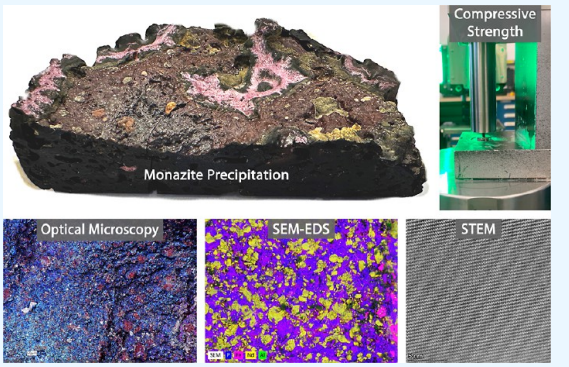

1. INTRODUCTION

Around the globe, management of large volumes of nuclear waste has prompted research and development of various types of nuclear waste forms. These waste forms need to meet a wide range of physical and chemical criteria dictating their safety, stability, and longevity over very long time scales within geological repositories. Over the past several decades, waste management strategies have been studied for different types of nuclear waste ranging from U.S. Department of Energy legacy wastes including low-activity wastes[1−3] to international efforts for low-level and intermediate-level wastes (LILW)[4] and high-level wastes (HLW).[5,6] These strategies will also be crucial to management of future nuclear wastes from Generation IV (Gen IV) advanced nuclear reactor designs[7,8] and wastes that could be generated if the U.S. decides to reprocess used nuclear fuel and close the nuclear fuel cycle.[9−11] These wastes represent a broad range of physical and chemical forms, requiring detailed understanding of processing parameters, property characterizations, and modeling to achieve advanced solutions for effective immobilization and safe long-term storage. This work proposes a novel waste form for processing salt-based nuclear wastes and immobilizing the phosphate products in a multiphase glass-ceramic waste form.

One of the Gen-IV advanced reactor concepts is the molten salt reactor (MSR) that includes variations where the fuel is in salt form (e.g., chlorides, fluorides), which requires processing prior to storage and/or disposal.[12−14] This includes actinide removal at a minimum to prevent unwanted production of gaseous byproducts (e.g., UF_6).[15] Additionally, gaseous byproducts can be produced (e.g., $F_{2(g)}$)[15,16] through radiolysis, resulting in pressure hazards in storage tanks, which occurred during storage of the $LiF−BeF_2$ (FLiBe) salts from the Molten-Salt Reactor Experiment (MSRE) at Oak Ridge National Laboratory in the 1960s. Additionally, pyroprocessing of used EBR-II fuel at Idaho National Laboratory and Argonne National Laboratory has resulted in different salt-based nuclear wastes (i.e., LiCl−KCl + NaCl + fission products). Since these salt wastes are not compatible with traditional waste processing technologies to create the state-of-the-art HLW waste forms (i.e., vitrification to produce borosilicate glasses),[17] alternative processing strategies are needed. For effective long-term radioactive waste storage, a wide range of radionuclides must be efficiently isolated and immobilized in the waste form.

Received: April 30, 2025
Revised: July 2, 2025
Accepted: July 15, 2025
Published: July 22, 2025

https://doi.org/10.1021/acsomega.5c03993
ACS Omega 2025, 10, 33524−33535

On the other hand, real-time removal of neutron poison fission products from an MSR can improve reactor operation efficiency, including xenon isotopes (e.g., ^{135}Xe) and rare earth elements (REEs, e.g., ^{143}Nd, ^{147}Pm, ^{149}Sm, ^{157}Gd). The selective removal of noble gas fission products can be accomplished through cleaning of off-gas with a carrier gas and/or through sparging (e.g., He). REE removal can be achieved via electrochemical reduction (e.g., through lanthanide drawdown)[18] or chemical separation (e.g., reactive distillation[19] and oxidative precipitation).[20] In chemical separations, REEs can be recovered in the forms of oxide/oxyhalide (REO_x/REOCl) mixtures, which can be fully converted to oxide forms (RE_2O_3/REO_2)[21−24] or phosphate forms ($REPO_4$)[23] through subsequent treatments in oxidizing environments. Then, final immobilization of these products is required.

For the mixed REO_x form of this waste stream, the ideal waste form is a lanthanide (alumino)borosilicate (LABS) glass with REO_x loadings of >60 mass % and excellent chemical durability.[23,25−30] For the $REPO_4$ mixture, the ideal waste form is a combination of monazite (monoclinic $P2_1/n$ space group; La → Dy) and xenotime (tetragonal $I4_1/amd$ space group; Sc, Y, Gd → Lu) phases depending on the REEs present.[31] These $REPO_4$ compounds are compatible with demonstrated phosphate-based waste form technologies including glasses and crystallized glass systems.[32−34] Additionally, this family exhibits material properties well-suited to waste storage and occurs naturally in Th- and U-containing minerals. The main points for the utility of $REPO_4$ compounds as promising waste management candidates include, but are not limited to, the following:[35] (i) exceptional chemical stability in the Earth's crust over geological time scales;[36,37] (ii) potential to contain large fractions of actinide components (i.e., Th and U as well as compatibility with $PuPO_4$);[38] (iii) resistance to displacive irradiation damage;[39−41] (iv) low solubility in an aqueous environment at high temperatures;[42] (v) high chemical durability relative to borosilicate-based waste forms,[43] and (vi) high retention of fission products during erosion.[44]

In addition to borosilicate glasses, phosphate glasses (particularly iron phosphate and aluminophosphate glasses) have also been considered as effective waste forms due to their desirable processing and physical properties.[24,45] Iron phosphate glasses, in particular, have attracted attention due to their low melting temperature, high chemical durability, and high solubility of REEs and transition metal ions compared to other waste glasses. One challenge to studying iron phosphate glasses is that the iron redox ratio, which depends on the batch chemistry and melting conditions, can have large effects on the physical and chemical properties.[46−48] Alternative to classic high-temperature synthesis, low-temperature, one-step synthesis poses another pathway for generation of monazite-based nuclear waste forms.[49]

The current study aimed to synthesize a phosphate-based waste form suitable for salt waste processes (see above) to selectively generate $REPO_4$ byproducts. Specifically, the waste form was a glass-bonded $REPO_4$ waste form within a binary glass phase, $60P_2O_5$−$40Fe_2O_3$, a mixture that has demonstrated high chemical durability.[45,46,50] This was demonstrated at a 23 g scale with a 26 mass % Nd loading and then at 75 g and 1600 g scales with 37 mass % Nd loading. The samples were characterized microstructurally [i.e., optical microscopy (OM), scanning electron microscopy (SEM), and X-ray computed tomography (XCT)], crystallographically [i.e., X-ray diffraction (XRD) and electron backscatter diffraction (EBSD)], and compositionally [i.e., energy-dispersive X-ray spectroscopy (EDS)]. These analyses enabled the assessment of viability for large-scale laboratory synthesis via melt processing.

2. MATERIALS AND METHODS

2.1. Sample Preparation. In this study, three samples were prepared to represent simulated iron-phosphate- and monazite-based waste forms. The flow diagram describing the syntheses processes for each is provided in Figure 1. General

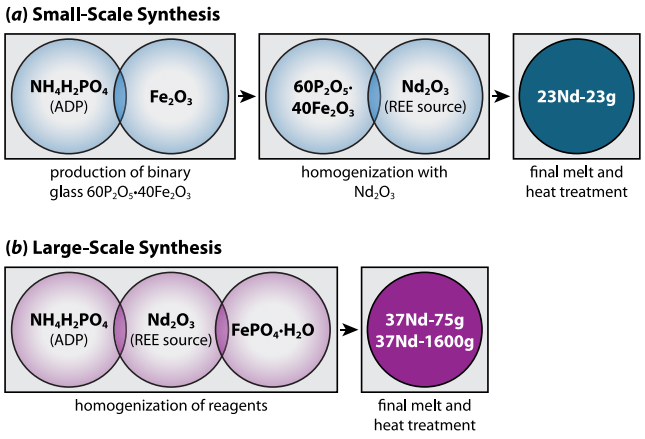

Figure 1. Process flow diagram showing the preparation of (a) the small-scale sample (26Nd-23g) and (b) the larger-scale samples (i.e., 37Nd-75g and 37Nd-1600g).

compositions in masses and fractions for these samples are provided in Table 1 along with details regarding the heat

Table 1. Details for the Production of the Samples 26Nd-23g, 37Nd-75g, and 37Nd-1600g, Including Both the Additives and the Final Composition[a]

	sample ID:	26Nd-23g	37Nd-75g	37Nd-1600g
category	target mass	23 g	75 g	1.6 kg
additives (g)	$NH_4H_2PO_4$	52.6828	45.5095	667.472
	$FePO_4·H_2O$	-	38.6556	506.503
	Fe_2O_3	17.4941	-	-
	Nd_2O_3	21.7627	47.3018	693.759
final composition (mass %)	Fe−P−O glass	56.88	38.81	38.81
	$NdPO_4$	43.12	61.19	61.19
	Nd	26	37	37
thermal treatment	t_{ADP} (h)	1	1	4
	t_{1000} (h)	-	1	4
	T_{max} (°C)	1300	1300	1300
	t_d (hr)	2	1	4
	V_{cruc} (mL)	250/40	100	4750
	annealing	545 °C, 48 h	not applied	not applied
	cooling	note[b]	furnace cooling	2 °C/min

[a]Included are details about the heat treatment process, including the time delay at 400 °C for ADP decomposition (t_{ADP}), the time delay at 1000 °C to allow $FePO_4$ to melt (t_{1000}), the max temperature for heat treatment (T_{max}), the dwell time at T_{max} (t_d), the crucible volume (V_{cruc}), and the annealing process (if applicable). Heating rates were 5 °C/min. [b]See Figure S1 for the cooling curve used for 26Nd-23g.

https://doi.org/10.1021/acsomega.5c03993
ACS Omega 2025, 10, 33524−33535

treatment processes. Specific details for each sample are given below in the subsections. The sample with 26% Nd-mass loading will be called 26Nd-23g. The samples with 36.9% Nd-mass loading will be called 37Nd-75g and 37Nd-1600g for 75 g and 1600 g samples, respectively.

2.1.1. 26Nd-23g Fabrication with the Fe−P−O Frit. For making the 26Nd-23g sample, a hold point was used at 400 °C for 1 h to minimize foaming from $NH_4H_2PO_4$ (ADP) decomposition as gases trapped inside of molten glass might result in additional voids/cracks inside of the final glass and to minimize the likelihood of the melt foaming out of the crucible. These structural imperfections might be further exacerbated by $NdPO_4$ crystallization, so a binary $60P_2O_5$−$40Fe_2O_3$ (by mole) glass was prepared beforehand as an additive. This glass was initially prepared by heating it at 5 °C min^{-1} to 400 °C to allow for ADP decomposition, and then the melt was then heated to 1300 °C, with a 2 h hold. The resulting glass was then quenched by pouring it on an Inconel plate at room temperature. The resulting amorphous binary glass was milled in a tungsten carbide mill, Nd_2O_3 was added, and the mixture was homogenized in the same mill. Afterward, the mixture was loaded into an alumina crucible (40 mL of CoorsTek, d = 25 mm, h = 100 mm, where d = diameter, and h = height) and was heated at a temperature profile provided in Figure S1. The temperature profile was designed to maximize the amount of evenly sized crystallites across the volume of the sample. Uncontrolled crystallization often leads to formation of voids, which may negatively impact final properties of the sample, e.g., lower compressive strength.

2.1.2. 37Nd-75g and 37Nd-1600g Fabrications. While the preparation of binary $60P_2O_5$−$40Fe_2O_3$ glass for 26Nd-23g resulted in a mechanically sound sample with mitigated presence of large crystallites and voids, this approach in a laboratory environment was not deemed feasible for the production of large-scale samples due to the limitation due to equipment sizes and safety concerns with doing a quench of such a large volume of phosphate melt in a fragile alumina crucible (i.e., they can crack due to thermal shock). For these reasons, the 37Nd-75g and 37Nd-1600g samples were prepared by mixing raw materials instead of a premade frit with reagents. For samples 37Nd-75g and 37Nd-1600g, mixtures of $FePO_4{\cdot}H_2O$, ADP, and Nd_2O_3 were used to reduce the volume expansion associated with decomposition of ADP (in contrast to where all P was provided only by ADP for the 26Nd-23g sample).

Both samples were prepared by weighing and homogenizing the source materials in alumina crucibles. The temperature profile was designed to maximize the precipitation of monazite crystals and is provided in Figure S2. The key differences between these two samples were the batch sizes, crucibles, and heat treatments used. The 37Nd-75g sample was made at a 75 g batch size in a CoorsTek crucible (65539) with dimensions of d = 35 mm and h = 64 mm, and the 37Nd-1600g sample was made in a CoorsTek crucible (65548) with dimensions of d = 178 mm and h = 228 mm. The reaction for this mixture of $FePO_4$ (simplified as a nonhydrate), ADP, and Nd_2O_3 to form the binary $60P_2O_5$−$40Fe_2O_3$ glass and $NdPO_4$ (monazite) is shown below in eq 1.

$$0.80\,FePO_4 + 1.38\,NH_4H_2PO_4 + 0.49\,Nd_2O_3 \rightarrow 1.00[0.4\,Fe_2O_3{\cdot}0.6\,P_2O_5] + 0.98\,NdPO_4 + 1.38\,NH_3 + 2.07\,H_2O \quad (1)$$

2.2. Sample Characterization. *2.2.1. XRD Analysis.* Samples for the XRD analysis were performed by milling the sample in a tungsten carbide mill. In the case of 37Nd-1600g, spatial variations of the glass composition and structure were expected due to uneven heating across these regions of the sample due to slower heat transfer toward the centerline. To characterize these variations, subsamples were sliced from different regions with a diamond saw and ground with the tungsten carbide mill. XRD analyses were performed using a Bruker D8 Advance X-ray diffractometer with a Cu Kα X-ray source with 40 kV and 40 mA operating conditions. A LynxEye position-sensitive detector was utilized in 1-D mode where measurement parameters were 5−90° 2θ with a 0.15° 2θ step and 0.1-s dwell times per step. The identified patterns were found using ICDD PDF2 2019. The Rietveld refinement was done by addition of 5 mass % of CeO_2 (NIST SRM-674b) to the original sample so that the amorphous fraction could be calculated, and phases were matched with crystallographic information files from the Inorganic Crystal Structure Database (ICSD).

2.2.2. Scanning Electron Microscope Analysis. To prepare samples for SEM analysis, all sample cuts were made with a Buehler Isomet low-speed saw using a diamond blade and a Buehler Isocut coolant. In the case of the 37Nd-1600g sample, samples were collected similarly to those used for XRD analysis. Polished samples were coated under vacuum with a 2.5-nm layer of Ir by thermal evaporation using a Quorum Technologies EMS 150 T ES Iridium Sputter coater. SEM analyses were conducted with a JEOL model JSM-7001F.

2.2.3. Energy-Dispersive Spectroscopy and Electron Backscatter Diffraction (EBSD) Analyses. The JSM-7001F SEM was equipped with Bruker EDS and EBSD detectors (Bruker AXS Inc., Madison, WI). Chemical composition and elemental dot maps were collected using a Nano xFlash 6|60 EDS detector at an acceleration voltage of 15 kV and collected with a Bruker Esprit 2.3. The EBSD data was obtained on specimen polished with diamond suspensions down to 1 μm with an e-FlashHD EBSD detector used at an acceleration voltage of 25 kV.

2.2.4. Scanning Transmission Electron Microscopy with EDS. A cross-sectional scanning transmission electron microscopy (STEM) sample was prepared using a Thermo Fisher Quanta 3D FEG Dual-Beam Ga^+ focused ion beam−SEM (FIB-SEM) with a standard liftout procedure.[51] STEM images were acquired on two probe-corrected instruments, a JEOL ARM-200CF operating at 200 kV, and a Themis Z operating at 300 kV. Convergence semiangles were 27.5 and 25 mrad, respectively, while collection angles ranged between 65 and 280 mrad for high-angle annular dark field. Beam currents and dwell times were minimized to reduce the extent of sample damage. STEM energy-dispersive X-ray spectroscopy (EDS) composition maps were acquired by using a SuperX detector. Lines cans were obtained after integrating 68 pixels using ThermoFisher Velox software.

2.2.5. Compressive Strength Testing. Compressive strength tests were run in triplicate on an Instron 5582 (ID 5582R1924) using a fixed rate of 0.1 mm/min in accordance with ASTM C1358-18.[52] Samples were prepared as rectangular prisms in a 2:1 geometry of height/(width, depth) with general dimensions of ≈6 mm × ≈3 mm × ≈3 mm using a diamond wire saw. Samples were loaded until failure, and the compressive strength was reported as the maximum uniaxial compressive stress reached when the material failed.

https://doi.org/10.1021/acsomega.5c03993
ACS Omega 2025, 10, 33524−33535

2.2.6. Chemical Durability Testing. All chemical durability samples in this report were prepared according to the ASTM C1220-21[53] procedure (also called MCC-1). The reaction vessels were 60 mL of PFA (perfluoroalkoxy alkane) jars from Savillex that were cleaned per the ASTM C1220-21 procedure. The vessels were equipped with a meshed PFA basket to support the coupon and Teflon tape around the threading to reduce the evaporation rate of deionized water (DIW) from the vessel.

The samples were inserted each into the individual basket, and the vessels were filled with DIW (>18.0 MΩ-cm) to obtain surface-area-of-glass-to-solution-volume of SA/V = 10 m^{-1}. The SA values of the coupons were obtained with XCT, as described below since these samples contained pores, with a Zeiss Xradia Versa 610 X-ray microscope. Collection was done at 160 kV, 25 W, 8 s collection times per projection, and 2401 projections around a full 360°. An appropriate filter was utilized to maximize transmission through the material. A 0.4× objective lens set to 2 × 2 binning of the camera was selected in conjunction with the source and detector positioning to provide a 20.5 μm voxel size.

The vessels were maintained at 90 ± 2 °C. On the date of solution collection, 0.25 mL of solution was collected and preserved in 2.75 mL of 0.3 M HNO_3 to meet the minimal sample volume requirements dictated by the analytical laboratories. Samples were analyzed quantitatively using a PerkinElmer Optima 8300 dual-view inductively coupled plasma-optical emission spectrometer (ICP-OES) with a PerkinElmer S-10 autosampler interface. More information about the analytical process is provided in the Supporting Information. The normalized release (NL_i) for element "i" over the time period is based on eq 2, where m_i is the total mass of element released from the glass at the time (t_n, in g), s_{glass} is the surface area of glass exposed to the DIW (in m^2), and f_i is the mass fraction of element in the glass (unitless).[54]

$$NL_i = \frac{m_i(t_n)}{s_{glass} \times f_i} \quad (2)$$

3. RESULTS

3.1. Appearances. Pictures of the three samples are provided in Figure 2. Each of the samples appears similar in color with notable differences in residual phases, porosities, and microstructures. The 26Nd-23g sample appeared as a homogeneous and mostly consolidated glass-ceramic product, and the sample had lower porosity than the other two higher-Nd samples.

3.2. Phase Distribution. The XRD analyses revealed two different crystal phases, i.e., $NdPO_4$ (monazite, ICSD 79750) and $Fe_3(P_2O_7)_2$ (ICSD 71129), and the results are presented in Table 2. When comparing the XRD results, we consider variation in starting chemistry between 26Nd-23g and the high-loading samples (37Nd-75g and 37Nd-1600g), time–temperature history (see Section 2.1), crucible geometry, and batch size (see Table 1). Comparing 37Nd-75g with 37Nd-1600g illustrates the impact of different crucible geometries on the final product. The 37Nd-75g contained ∼50 mass % of $NdPO_4$, the rest of the sample appeared amorphous. In the case of 37Nd-1600g, an additional crystalline phase appeared, $Fe_3(P_2O_7)_2$, similar to that of 26Nd-23g. The fraction of amorphous phase in this sample is also significantly lower than for 37Nd-75g. One explanation for this increased crystallization is the difference in total heat treatment time. While the total heat treatment time of 26Nd-23g took ≈108 h total, and was by far the longest, the preparation of 37Nd-75g only took ≈24 h and 37Nd-1600g took ≈33 h. The programmed steps on the controller of furnace may accurately define the ambient temperature of the furnace, but do not directly inform about temperature fields inside of the sample (i.e., the slowest cooling region is the centerline). This likely explains why the central region of 37Nd-1600g (the slowest cooling) demonstrated much lower amorphous phase amount compared to outer and surface parts of the sample (fastest cooling). Table 2 also includes the R_{wp} (weighted profile R-factor), which is provided to evaluate the goodness-of-fit for the refinement.

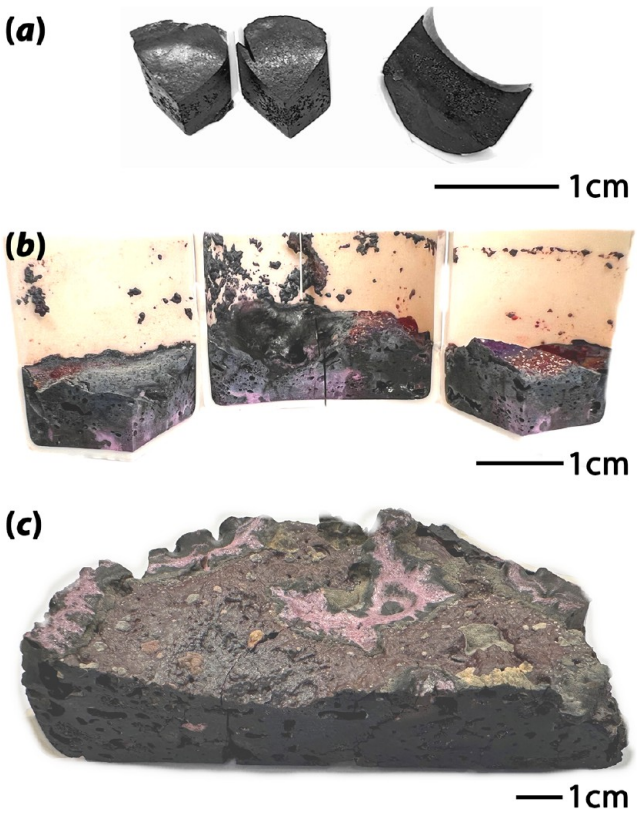

Figure 2. Pictures of samples: (a) a cross-sectional view of 26Nd-23 (mostly) broken out of the crucible, (b) a cross-sectional view of 37Nd-75g still in the crucible, and (c) a cross-sectional view of 37Nd-1600g broken out of the crucible. Each image has a separate scale bar.

3.3. Chemical Durability. Chemical durability results for the samples focused on the dissolution of phosphorus as the primary glass-forming element of the matrix. Data points collected for this work include up to 210 days for 26Nd-23g and up to 28 days for 37Nd-1600g. The MCC-1 test data sets for 26Nd-23g and 37Nd-1600g are compared with similar iron phosphate waste forms that were also slow-cooled following their homogenization at high temperatures in Figure 3. These other samples contained mixed-lanthanide monazite [i.e., $(Ce,Nd)PO_4$] based on SEM-EDS analyses but also contain several additional cations (e.g., Li, K, Na, Cs, Sr, and Ce) using a more complex waste simulant, and the data are presented elsewhere.[56,57]

3.4. SEM-EDS-EBSD Results. The SEM-EDS data for 26Nd-23g are listed in Figure 4a–e. These reveal a minor amount of alumina present in the sample from crucible dissolution within the sample matrix, which has been observed

https://doi.org/10.1021/acsomega.5c03993
ACS Omega 2025, 10, 33524−33535

Table 2. Rietveld Refinement for the Three Samples Where Values Are in Mass %[a]

sample ID	location	$NdPO_4$ (ICSD 79750)	$Fe_3(P_2O_7)_2$ (ICSD 71129)	amorphous	R_{wp}
26Nd-23g	full	19.7	40.9	39.3	6.1
37Nd-75g	bottom	53.1	-	46.9	6.1
	top	50.5	-	49.5	5.8
37Nd-1600g	top center	62.1	10.6	27.3	4.3
	top radius	34.1	30.8	35.1	5.9
	top edge	47.5	31.4	21.1	5.7
	middle center	72.9	23.1	4.0	6.2
	middle radius	62.1	26.2	11.7	6.3
	middle edge	59.2	32.2	8.6	7.1
	bottom center	68.6	24.6	6.8	4.7
	bottom radius	74.8	23.2	2.0	4.8
	bottom edge	46.6	37.9	15.5	6.5

[a]The R_{wp} is the weighted profile *R*-factor,[55] a "goodness of fit" metric for the refinement.

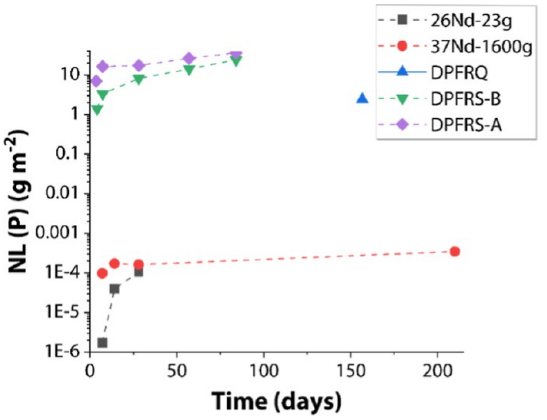

Figure 3. Summary of normalized phosphorus releases (NL_P) for samples from the literature (i.e., DPFRQ, DPFRS-A, and DPFRS-B)[56,57] as well as 26Nd-23g and 37Nd-1600g.

previously.[58,59] The SEM-EDS data for 26Nd-23g agree with the XRD showing the monazite distribution.

The 37Nd-1600g specimen also shows monazite crystals (Figure 5a–e). EBSD maps in Figure 6 confirm the identity of these crystals as $NdPO_4$. The inverse pole figure (IPFX) map in Figure 6d provides an image where the axes of the projection sphere are aligned with the *X*-direction, and the grain map in Figure 6c shows where different grains are located. While Figure 6b shows grain boundaries, the IPFX map in Figure 6d provides both grain boundary and grain orientation information. Together, these maps show that some of the crystals which appear in the SEM to be single crystal grains are actually polycrystalline agglomerates. Note that the difference between the phase used in XRD quantification [i.e., $Fe_3(P_2O_7)$] is different than the phase used for EBSD analysis [i.e., $Fe_2P_2O_7$] due to the phase databases used.

3.5. STEM-EDS Results. STEM-EDS analysis of the particles confirmed the monazite ($NdPO_4$) phase as shown in Figure 7 (see Figure S6, for more information). EDS maps were collected on a particle edge, with the plane parallel to the particle–glass interface identified as (200). There was a bimodal distribution of the glass matrix with both amorphous and crystalline regions that showed a clear difference in Fe and

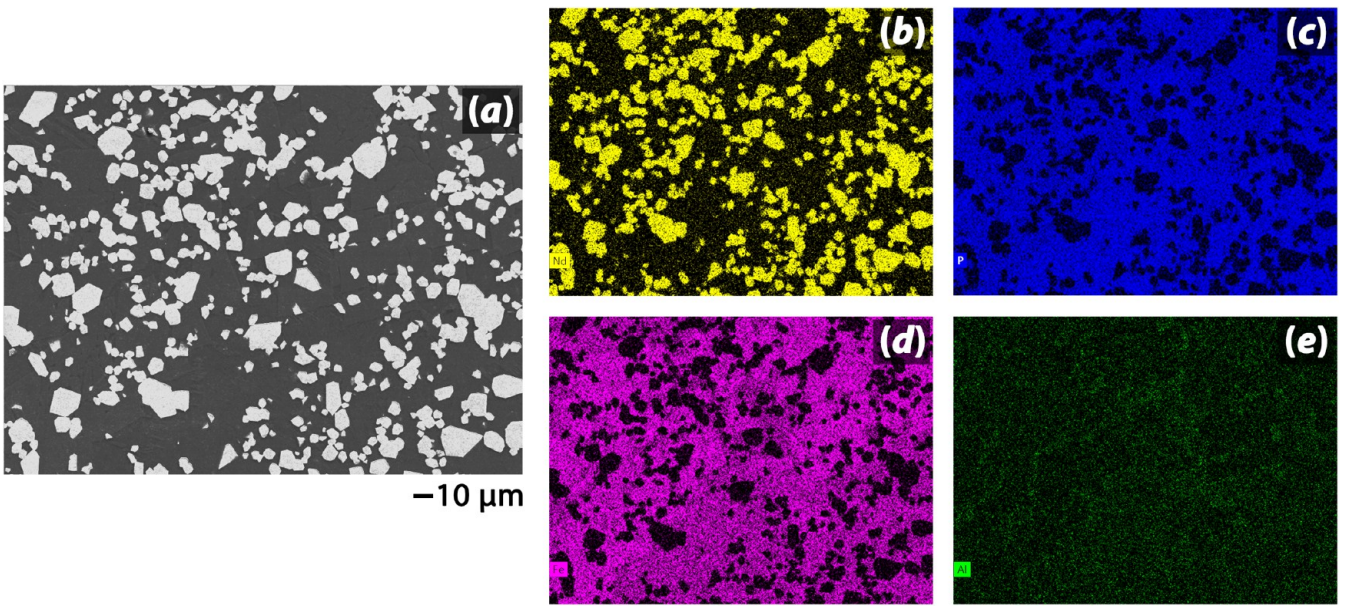

Figure 4. SEM-EDS collage of the 26Nd-23g sample under 500× magnification, including (a) an SEM micrograph (white phase is monazite), as well as (b–e) EDS dot maps for (b) Nd, (c) P, (d) Fe, and (e) Al (contamination from the alumina crucible).

https://doi.org/10.1021/acsomega.5c03993
ACS Omega 2025, 10, 33524–33535

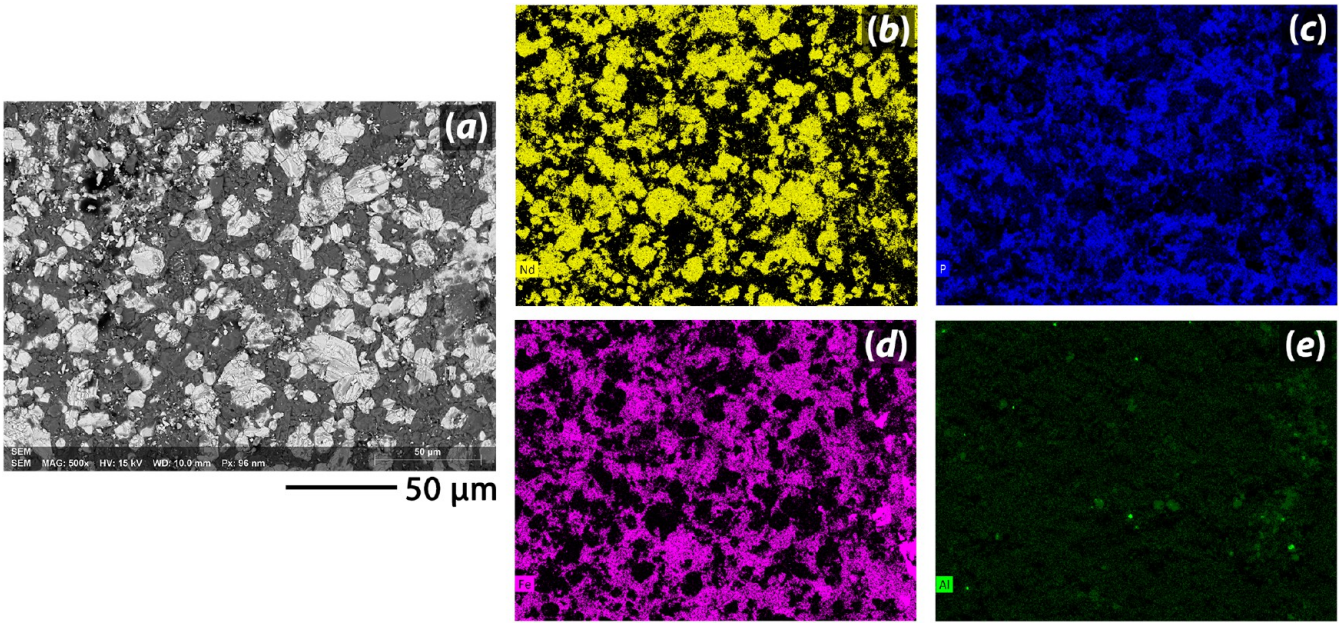

Figure 5. SEM-EDS collage of the 37Nd-1600g sample (bottom-radius) under 500× magnification, including (a) an SEM micrograph (the white phase is monazite), as well as (b−e) EDS dot maps for (b) Nd, (c) P, (d) Fe, and (e) Al (contamination from the alumina crucible).

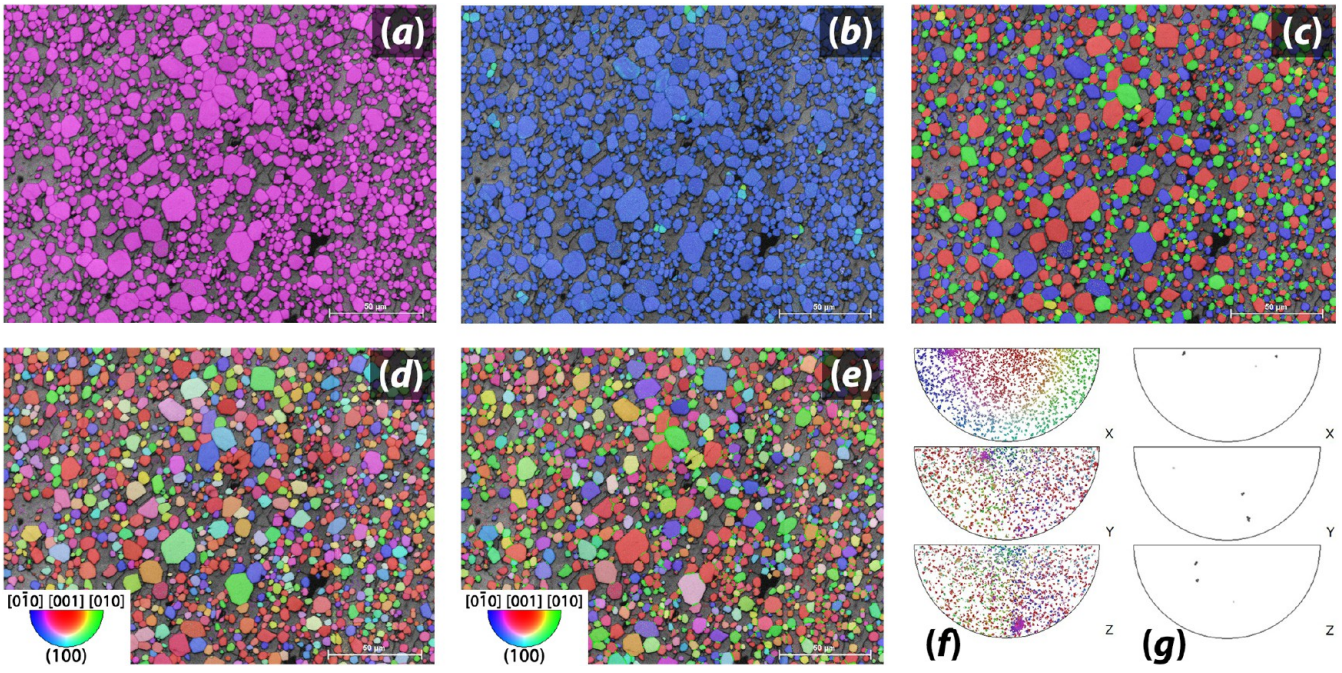

Figure 6. EBSD data for 37Nd-1600g (bottom—center), including (a) the phase map, (b) misorientation map, (c) grain map, (d) the inverse pole figure (IPFX) map with corresponding color scheme, (e) the inverse pole figure (IPFY) with the corresponding color scheme, (f) the pole figure for monazite orientations, and (g) the pole figure for $Fe_2P_2O_7$ orientations.

P concentrations across the boundary in the middle; the concentration gradient can also be seen by fluctuations in the P and Fe concentrations shown in the elemental maps (see Figure 7e,f, respectively). Crystalline regions appeared primarily at the particle boundaries. While efforts were made during FIB preparation to avoid beam damage, it is difficult to determine whether Ga^+ damage induced the transformation or if this structure existed prior to the FIB liftout.

4. DISCUSSION

Figure 8a−i provides an overview of the large-mass sample produced, i.e., 37Nd-1600g, including the pictures of compressive strength coupons, the optical microscopy of the slide through the middle, a picture of the chemical durability testing coupon, multiple images of the sample cut in half, and an XCT view of the sample still within the crucible, as well as some SEM-EDS and STEM data. This information was discussed above in more detail but is summarized here for an overview of the characterizations performed on this sample.

https://doi.org/10.1021/acsomega.5c03993
ACS Omega 2025, 10, 33524−33535

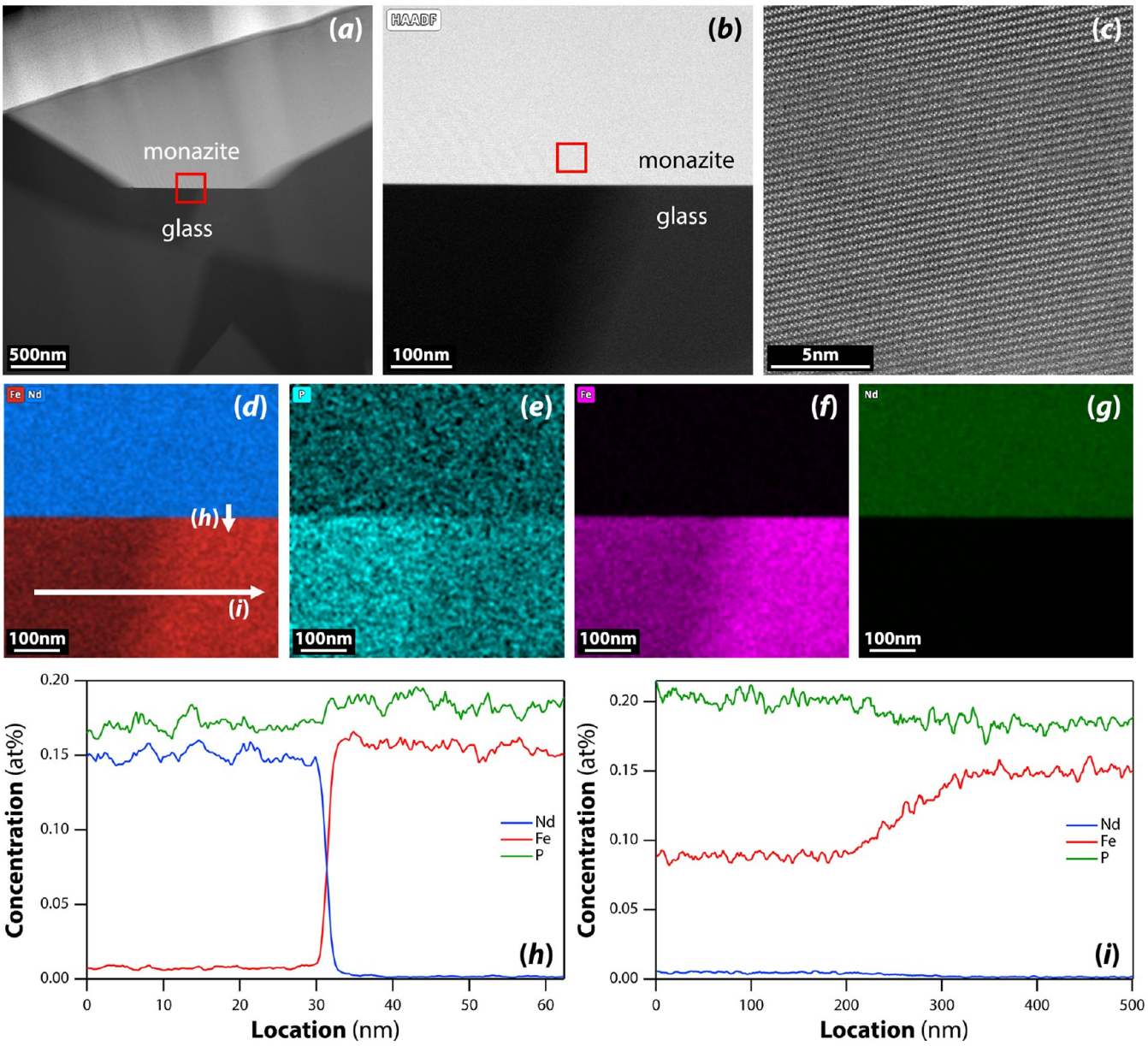

Figure 7. STEM-EDS collage showing (a−c) STEM micrographs at different magnifications at and near the monazite−glass interface, (d−g) EDS elemental maps at the field of view in (b) and overlays for (d) Fe + Nd, (e) P, (f) Fe, and (g) Nd as well as (h,i) line scans performed at the locations shown with arrows in panel (d) (arrows drawn to scale) to provide elemental fluctuations of Nd, Fe, and P. Note that (b) is a magnified view of the box in (a) and (c) is a magnified view of the box in (b).

$REPO_4$ (i.e., monazite and xenotime) compounds show promise as waste forms for REEs as their salt cation loadings are very high, and they have ideal waste form properties, including high chemical durabilities.[31] Defining a maximum waste loading criterion for a particular waste form requires a holistic assessment of thermal, mechanical, and chemical durability properties pertaining to stability during long-term geological storage. These properties are affected not only by the chemical composition but also the distribution of mineral and amorphous phases present within multiphase waste form. While these properties are easily correlated in smaller-scale (<75 g) laboratory samples, several questions remain unclear, including differing properties for scaled-up waste form (engineering-scale vs bench-scale) production, property relationships for differing geometries, and changes in mineral phase distributions due to heterogeneous temperature distributions during cooling.

In the Nd−Fe−P−O amorphous melt, P serves as the network-forming element, and Nd and Fe serve as network modifiers and/or intermediates. Previous studies reported that addition up to 15 wt % of Nd_2O_3 would result in amorphous waste form.[23] Beyond this addition, increasing the addition of network modifiers/intermediates can result in the precipitation of crystal phases as reported by Liu et al.[60] A similar trend was observed in the current study with an increased precipitation of $NdPO_4$ and $Fe_3(P_2O_7)_2$. It is important to note that, while precipitation of $Fe_3(P_2O_7)_2$ from $40Fe_2O_3{-}60P_2O_5$ glass melts appears to be the most thermodynamically viable option, the presence of $Fe_3(P_2O_7)_2$ also depends on the time−temperature profile of the material preparation and atmosphere used.[61]

https://doi.org/10.1021/acsomega.5c03993
ACS Omega 2025, 10, 33524−33535

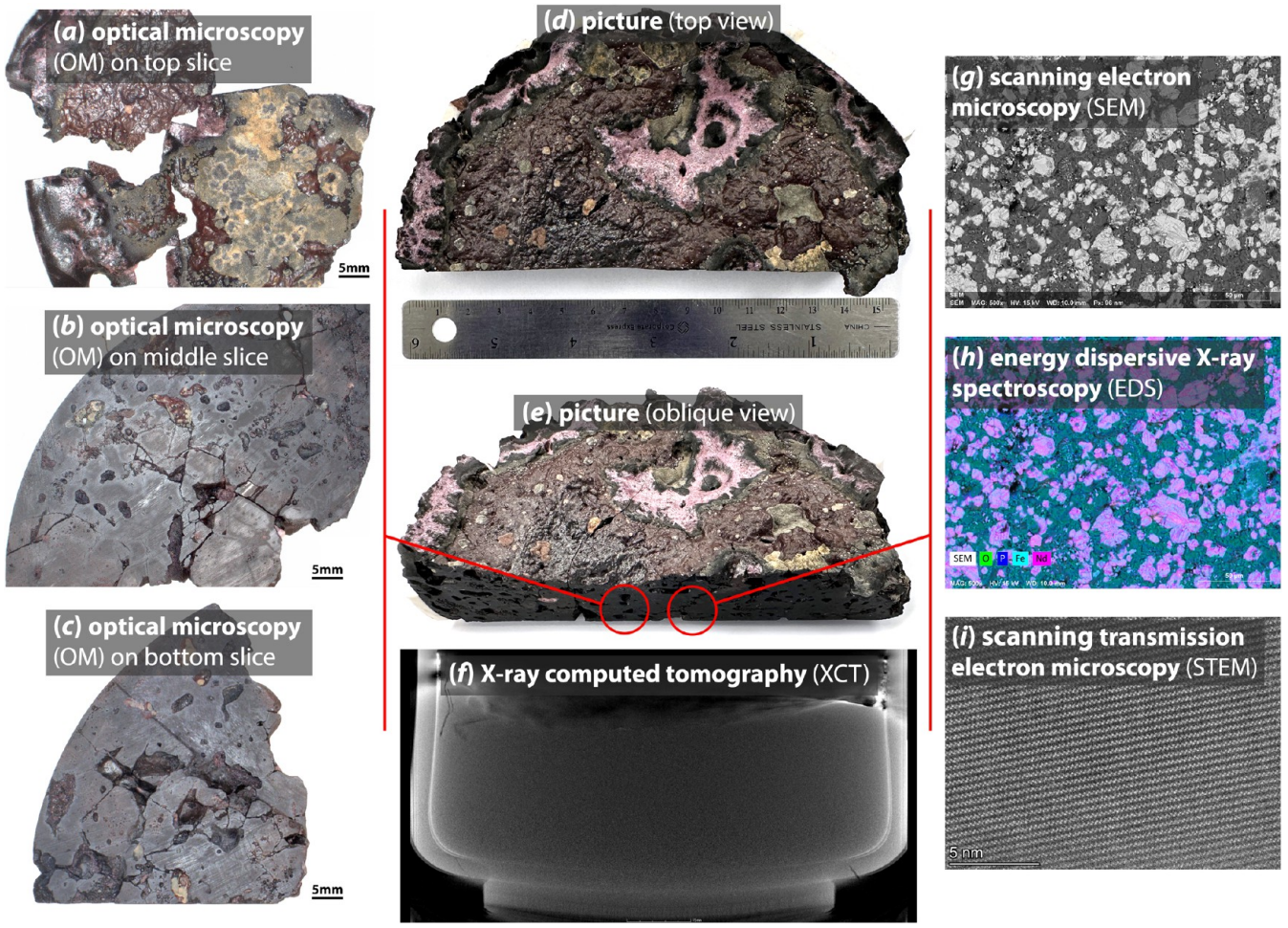

Figure 8. Summary of results from scale-up sample 37Nd-1600g showing (a−c) cross-sectional views of the slices from the full sample, (d,e) pictures the full sample at different angles (top down and oblique views, respectively), (f) XCT image of the sample still within the crucible, (g) SEM micrograph, (h) EDS elemental overlay, and (i) STEM micrograph of the sample.

Compressive strength results are also influenced by a wide range of material properties and sample preparation strategies. Examples of factors that introduce variabilities in compressive strength data include heterogeneities, cracks, and voids inside of the material and the degree of parallelism for opposing prism faces. Since it is likely that all these sample irregularities will decrease the overall performance of the coupon, the property values for an ideal sample are likely higher than those presented in Figure S5. However, these flaws are inherent in manufacturing strategies and the technological approach used for waste form production. Despite the challenges associated with manufacturing larger-scale samples and the resulting increase in structural flaws, the 1600 g sample exhibited nearly quadruple the compressive strength of the 23 g sample (≈194 ± 59 MPa for 37Nd-1600g vs 56 ± 27 MPa for 26Nd-23g, respectively). The increased structural flaws in 37Nd-1600g, likely caused by the higher monazite content (leading to mismatching in coefficients of thermal expansion), seem to be more than compensated for by the increase in monazite crystal content. This compressive strength value is still significantly lower value than that of pure engineered monazite materials[62] but it represents an exceptionally high value for kg-scale waste form samples synthesized with little-to-no control over the synthesis beyond the ambient temperature standpoint. Existing literature on monazite addition to composites[63−65] assumes that, due to the low hardness of monazite crystals, the induced stresses are deflected, resulting in higher energy demand for the propagation of cracks. Hay et al.[65] reported on the dislocation plasticity and twinning in monazite crystals as the likely mechanisms in indentation and fiber push tests. It is important to note that in complex polycrystalline matrices such as 26Nd-23g and 37Nd-1600g, these mechanisms will likely be accompanied by other material toughening mechanisms associated with the crystalline character of the matrix.

Assuming the low dissolution rates from the amorphous phase and from monazite,[33] the main contributor to the P release is likely the Fe-rich $Fe_3(P_2O_7)_2$ phase.[34,45,66] On average, 26Nd-23g contains a higher amount of $Fe_3(P_2O_7)_2$ than the other two samples, and while the dissolution rates for both samples appear to be reasonably similar, the amount of P appears to be initially higher for 37Nd-1600g. This could be the result of overall higher crystallinity within this sample and hence a lower amount of amorphous solid phase encapsulating the crystalline material. It is also important to note that while the *SA* values of 26Nd-23g and 37Nd-1600g were obtained via XCT, the more complicated *SA* of 37Nd-1600g (due to complex porosity) translates to higher uncertainty in the initial and long-term assessment of leaching. However, each of the presented materials has shown low dissolution rates of 8.68×10^{-6} g m^{-2} day^{-1} for 37Nd-1600g and 5.08×10^{-6} g m^{-2} day^{-1}

https://doi.org/10.1021/acsomega.5c03993
ACS Omega 2025, 10, 33524−33535

for 26Nd-23g. Figure 3 compares three waste forms: 26Nd-23g and 37Nd-1600g—both with highly simplified formulations—and the DPFRQ iron-phosphate-based waste stream, which has a far more complex chemical composition. The latter also underwent canister centerline cooling (a slow-cooling thermal profile similar to that of the samples in the current study), further altering its mineralogical structure. Due to this complexity, confirming the presence of monazite required both SEM-EDS and XRD, while quantification proved nearly impossible due to the large number of crystalline phases present and the heterogeneous nature of the samples. The overall mineralogical complexity and likely low abundance of chemically durable phases contributed to the poor durability observed in these samples. While this and other studies demonstrate strong long-term durability potential for monazite-containing waste forms, results from more realistic systems highlight the need to bridge these extremes and advance the design of iron-phosphate-based waste forms. If only REEs are present in a waste stream representative of the current study, the phase distribution would likely include xenotime as well as monazite depending on the specific REEs present.[59] Alternative to the processes described herein, a low-temperature process could be used to convert the REEs in the waste salt into $REPO_4$ compounds using a process documented by Zhoujin et al.[49]

Finally, the potential of phosphate-based material preparation on a large-scale basis needs to consider material compatibility from start to finish. The go-to containments for phosphate melt processing include ceramics like alumina or alumina-zirconia-silica (AZS),[60,67,68] which have demonstrated high affinity to the matrix itself. Basically, the refractory materials will be corroded and dissolve into the melt over time. The resulting chemistry change in the melt composition needs to be considered in property predictions for the final waste form performance. Dissolution of the crucible material may significantly alter material properties, especially during long-duration melt cycles, and make further behavioral predictions (i.e., via artificial intelligence and/or machine learning)[32] difficult due to these uncertainties.

5. SUMMARY AND CONCLUSIONS

The traditional approach in nuclear waste form development has historically consisted of picking one particular matrix for a given waste stream, where this matrix has then been continuously developed until the key benchmark properties were met. However, this approach always leaves unanswered questions about potential further improvement and, more importantly, about the versatility of the chosen matrices for different chemical/waste compositions in the broader range of future expansion toward new areas. The efficiency of nuclear waste cleanup could be enhanced by the creation of an immobilization "toolbox" strategy that leverages both data-driven and experimental methods to simultaneously evaluate relevant properties across many matrices for a given waste stream rather than focusing on a single matrix (e.g., borosilicate glass). The current work was conducted with the intent of producing multiphase waste forms, i.e., a high-durability crystalline material (Nd-monazite or $NdPO_4$) immobilized within a high-durability glass matrix ($60P_2O_5$–$40Fe_2O_3$).

The results presented within this paper show development for iron-phosphate waste forms that could be part of a potential "toolbox" strategy for future waste form design and production. The glass-bonded monazite waste forms were produced at 23 g scale for 26 mass % Nd loading, 75 g scale for 37 mass % Nd loading, and then at a much larger scale of 1600 g for the 37 mass % Nd loading. These materials show favorable chemical durabilities with high compressive strengths, despite the tested coupons containing some residual porosity. The 1600 g sample showed evidence of different phase distributions by location within the sample, which are attributed to the differing cooling rates after the primary heat treatment process. These differences will increase in complexity with increased batch sizes.

Iron-phosphate waste forms could be utilized for nuclear waste cleanup in the form of ceramics and glass ceramics. It is important to note that the properties of these waste forms depend heavily upon the microstructural and chemical distributions and consistencies, and these properties are directly related to the time−temperature history from material preparation. The realistic description of the true thermal history of samples such as these is difficult to predict when phase transformation and crystallization occur during cooling in addition to void production due to differences in coefficients of thermal expansion. With all of these things considered, it is still possible to create a high-efficiency waste form production process yielding a waste form with very attractive properties.

■ ASSOCIATED CONTENT

Data Availability Statement

The original contributions presented in this study are included in the article, further inquiries can be direct to the corresponding author.

Supporting Information

The Supporting Information is available free of charge at https://pubs.acs.org/doi/10.1021/acsomega.5c03993.

Sample production details, nuclear waste overview, process for cutting coupons from samples, compressive strength measurement information, density measurement information, additional information about ICP-OES characterization, and additional STEM-EDS data (PDF)

■ AUTHOR INFORMATION

Corresponding Author

Brian J. Riley − *Pacific Northwest National Laboratory, Richland, Washington 99334, United States;* orcid.org/0000-0002-7745-6730; Phone: +1 (509) 372-4651; Email: brian.riley@pnnl.gov

Authors

Miroslava Peterson − *Pacific Northwest National Laboratory, Richland, Washington 99334, United States*

Xiaonan Lu − *Pacific Northwest National Laboratory, Richland, Washington 99334, United States*

Kayla H. Yano − *Pacific Northwest National Laboratory, Richland, Washington 99334, United States;* orcid.org/0000-0002-8182-5439

Semanti Mukhopadhyay − *Pacific Northwest National Laboratory, Richland, Washington 99334, United States*

Ian I. Leavy − *Pacific Northwest National Laboratory, Richland, Washington 99334, United States*

Ethan K. Nickerson − *Pacific Northwest National Laboratory, Richland, Washington 99334, United States*

Robert J. Seffens − *Pacific Northwest National Laboratory, Richland, Washington 99334, United States*
Jincheng Du − *University of North Texas, Denton, Texas 76203, United States;* orcid.org/0000-0003-4805-7498
Kyle D. Miller − *Citrine Informatics, Redwood City, California 94063, United States*
James E. Saal − *Citrine Informatics, Redwood City, California 94063, United States;* orcid.org/0000-0003-0935-158X

Complete contact information is available at: https://pubs.acs.org/10.1021/acsomega.5c03993

Author Contributions

M.P., B.J.R., X.L., K.H.Y., S.M., I.I.L., E.K.N., R.J.S., J.D., K.M., and J.S. participated in the preparation of the original draft. All authors listed have made a substantial, direct, and intellectual contribution to the work and approved it for publication.

Notes

The authors declare no competing financial interest.

■ ACKNOWLEDGMENTS

The information, data, or work presented herein was funded in part by the Advanced Research Projects Agency-Energy (ARPA-E), U.S. Department of Energy, under Award Number DE AR0001613. The views and opinions of authors expressed herein do not necessarily state or reflect those of the United States Government or any agency thereof. Pacific Northwest National Laboratory (PNNL) is operated by Battelle Memorial Institute for the DOE under contract DE-AC05-76RL01830. The authors gratefully acknowledge John Vienna for project leadership as well as Jaime George and Derek Cutforth for their invaluable assistance in the setup of the new furnace used for the upscaling test. Their technical expertise and dedication were instrumental in ensuring the successful implementation of this critical aspect of the study. The authors thank Jincheng Bai for his expertise and offered insight during the internal review process.

■ REFERENCES

(1) Asmussen, R. M.; Fang, Y.; Tartakovsky, G. D.; Song, X.; Westsik, J. J. H.; Smith, G. L. *Performance Metric for Cementitious Waste Form Inventory Release in the Integrated Disposal Facility, PNNL-28992*; Pacific Northwest National Laboratory: Richland, WA, 2019.
(2) Marcial, J.; Riley, B. J.; Kruger, A. A.; Lonergan, C. E.; Vienna, J. D. Hanford low-activity waste vitrification: A review. *J. Haz. Mater.* **2024**, *461*, 132437.
(3) Saslow, S. A.; Um, W.; Russell, R. L.; Wang, G.; Asmussen, R. M.; Sahajpal, R. *Updated Liquid Secondary Waste Grout Formulation and Preliminary Waste Form Qualification, PNNL-26443; RPT-SWCS-009 Pacific Northwest*; National Laboratory: Richland, WA, 2017.
(4) McCloy, J. S.; Riley, B. J.; Dixon Wilkins, M. C.; Evarts, J. S.; Bussey, J.; Vienna, J. D.; Bingham, P. A.; Gregg, D. J.; Ojovan, M.; Schuller, S.; Uruga, K.; Perret, D.; Regnier, E.; Giboire, I.; Um, W.; Xu, K.; Goel, A.; Kruger, A. A. International perspectives on glass waste form development for low-level and intermediate-level radioactive waste. *Mater. Today* **2024**, *80*, 594−618.
(5) Goel, A.; McCloy, J. S.; Pokorny, R.; Kruger, A. A. Challenges with vitrification of Hanford High-Level Waste (HLW) to borosilicate glass—An overview. *J. Non-Cryst. Solids X* **2019**, *4*, 100033.
(6) Harrison, M. T. Vitrification of High Level Waste in the UK. *Proc. Mater. Sci.* **2014**, *7*, 10−15.
(7) Locatelli, G.; Mancini, M.; Todeschini, N. Generation IV nuclear reactors: Current status and future prospects. *Energy Policy* **2013**, *61*, 1503−1520.
(8) Zohuri, B. Generation IV nuclear reactors. In *Nuclear Reactor Technology Development and Utilization*; Khan, S. U.-D., Nakhabov, A., Eds.; Woodhead Publishing, 2020; pp 213−246.
(9) Adamov, E. O.; Mochalov, Y. S.; Rachkov, V. I.; Khomyakov, Y. S.; Shadrin, A. Y.; Kascheev, V. A.; Khaperskaya, A. V. Spent Nuclear Fuel Reprocessing and Nuclear Materials Recycling in Two-Component Nuclear Energy. *Atomic Energy* **2021**, *130*, 29−35.
(10) Sood, D. D.; Patil, S. K. Chemistry of nuclear fuel reprocessing: Current status. *J. Radioanal. Nucl. Chem.* **1996**, *203*, 547−573.
(11) Vienna, J. D.; Collins, E. D.; Crum, J. V.; Ebert, W. L.; Frank, S. M.; Garn, T. G.; Gombert, D.; Jones, R.; Jubin, R. T.; Maio, V. C.; Riley, B. J.; Nenoff, T. M.; Sevigny, G. J.; Soelberg, N. R. *Closed Fuel Cycle Waste Treatment Strategy, INL/EXT-15-34504*; Idaho National Laboratory: Idaho Falls, ID, 2015.
(12) Carlson, K.; Gardner, L.; Moon, J.; Riley, B.; Amoroso, J.; Chidambaram, D. Molten salt reactors and electrochemical reprocessing: synthesis and chemical durability of potential waste forms for metal and salt waste streams. *Int. Mater. Rev.* **2021**, *66*, 339−363.
(13) Riley, B. J.; McFarlane, J.; DelCul, G. D.; Vienna, J. D.; Contescu, C. I.; Forsberg, C. W. Molten salt reactor waste and effluent management strategies: A review. *Nucl. Eng. Des.* **2019**, *345*, 94−109.
(14) Serp, J.; Allibert, M.; Beneš, O.; Delpech, S.; Feynberg, O.; Ghetta, V.; Heuer, D.; Holcomb, D.; Ignatiev, V.; Kloosterman, J. L.; Luzzi, L.; Merle-Lucotte, E.; Uhlíř, J.; Yoshioka, R.; Zhimin, D. The molten salt reactor (MSR) in generation IV: Overview and perspectives. *Prog. Nucl. Energy* **2014**, *77*, 308−319.
(15) Del Cul, G. D.; Icenhour, A. S.; Simmons, D. W.; Trowbridge, L. D.; Williams, D. F.; Toth, L. M.; Dai, S. Overview of the recovery and processing of ^{233}U from the Oak Ridge molten salt reactor experiment (MSRE) remediation activities. In *Proc. Global 2001 International Conference on Back-End of the Fuel Cycle: From Research to Solutions*. 2001.
(16) Davis, L.; Hania, R.; Boomstra, D.; Rossouw, D.; Charpin-Jacobs, F.; Uhlir, J.; Maracek, M.; Beckers, H.; Riedel, S. Radiolytic Production of Fluorine Gas from MSR Relevant Fluoride Salts. *Nucl. Sci. Eng.* **2023**, *197*, 633−646.
(17) Hrma, P. R. *Retention of Halogens in Waste Glass, PNNL-19361*; Pacific Northwest National Laboratory: Richland, WA, 2010.
(18) Pereira, C.; Maggos, L.; Figueroa, J.; Willit, J. *Development of a Pyroprocessing Flowsheet Model for Safeguards Analysis, M3FT-12AN040302*; Argonne National Laboratory: Lemont, IL, 2012.
(19) Eun, H. C.; Choi, J. H.; Cho, I. H.; Lee, T. K.; Kim, T. J.; Shin, J. S.; Park, H. S.; Ahn, D. H. Purification of LiCl−KCl eutectic waste salt containing rare earth chlorides delivered from the pyrochemical process of used nuclear fuel using a reactive distillation process. *J. Radioanal. Nucl. Chem.* **2016**, *307*, 1419−1427.
(20) Cho, Y.-Z.; Park, G.-H.; Yang, H.-C.; Han, D.-S.; Lee, H.-S.; Kim, I.-T. Minimization of eutectic salt waste from pyroprocessing by oxidative precipitation of lanthanides. *J. Nucl. Sci. Technol.* **2009**, *46*, 1004−1011.
(21) Cho, Y.-Z.; Yang, H.-C.; Park, G.-H.; Lee, H.-S.; Kim, I.-T. Treatment of a waste salt delivered from an electrorefining process by an oxidative precipitation of the rare earth elements. *J. Nucl. Mater.* **2009**, *384*, 256−261.
(22) Riley, B. J.; Pierce, D. A.; Crum, J. V.; Williams, B. D.; Snyder, M. M. V.; Peterson, J. A. Waste form evaluation for $RECl_3$ and REO_x fission products separated from used electrochemical salt. *Prog. Nucl. Energy* **2018**, *104*, 102−108.
(23) Riley, B. J.; Chong, S. Glass waste form options for rare-earth fission products from electrochemical reprocessing. *J. Non-Cryst. Solids* **2020**, *545*, 120161.
(24) Chong, S.; Riley, B. J. Thermal conversion in air of rare-earth fluorides to rare-earth oxyfluorides and rare-earth oxides. *J. Nucl. Mater.* **2022**, *561*, 153538.
(25) Vienna, J. D.; Schweiger, M. J.; Riley, B. J.; Smith, D. E.; Peeler, D. K.; Reamer, I. A. *Property Data for Simulated Americium/Curium*

Glasses, PNNL-13009; Pacific Northwest National Laboratory: Richland, WA, 1999.
(26) Vienna, J. D.; Smith, D. E.; Schweiger, M. J.; Riley, B. J.; Crum, J. V.; Peeler, D. K.; Edwards, T. B.; Reamer, I. A. *Composition/Property Relationships for the Phase I Am/Cm Variability Study (U), WSRC-TR-99-00055*; Westinghouse Savannah River Company, Savannah River Technology Center: Aiken, SC, 1999.
(27) Youchak-Billings, A. L.; Crum, J. V.; Marra, J. C.; Riley, B. J.; Vienna, J. D.; Edmondson, A. *Waste/Storage Form Baseline-Fission Products & Lanthanides, GNEP-WAST-PMO-MI-DV-2008-000151*; Savannah River National Laboratory: Aiken, SC, 2008.
(28) Crum, J. V.; Billings, A.; Lang, J. B.; Marra, J. C.; Rodriguez, C. P.; Ryan, J. V.; Vienna, J. D. *Baseline Glass Development for Combined Fission Products Waste Streams, AFCI-WAST-WAST-MI-DV-2009-000075, PNNL-18524*; Pacific Northwest National Laboratory: Richland, WA, 2009.
(29) Mohd Fadzil, S.; Hrma, P.; Schweiger, M. J.; Riley, B. J. Liquidus temperature and chemical durability of selected glasses to immobilize rare earth oxides waste. *J. Nucl. Mater.* **2015**, *465*, 657−663.
(30) Mohd Fadzil, S.; Hrma, P.; Schweiger, M. J.; Riley, B. J. Component effects on crystallization of RE-containing aluminoborosilicate glass. *J. Nucl. Mater.* **2016**, *478*, 261−267.
(31) Chong, S.; Riley, B. J.; Lu, X.; Du, J.; Mahadevan, T.; Hegde, V. Synthesis and properties of anhydrous rare-earth phosphates, monazite and xenotime: a review. *RSC Adv.* **2024**, *14*, 18978−19000.
(32) Hegde, V. I.; Peterson, M.; Allec, S. I.; Lu, X.; Mahadevan, T.; Nguyen, T.; Kalahe, J.; Oshiro, J.; Seffens, R. J.; Nickerson, E. K.; Du, J.; Riley, B. J.; Vienna, J. D.; Saal, J. E. Towards informatics-driven design of nuclear waste forms. *Dig. Disc.* **2024**, *3*, 1450−1466.
(33) Bohre, A.; Avasthi, K.; Pet'kov, V. I. Vitreous and crystalline phosphate high level waste matrices: Present status and future challenges. *J. Ind. Eng. Chem.* **2017**, *50*, 1−14.
(34) Day, D. E.; Ray, C. S. *A Review of Iron Phosphate Glasses and Recommendations for Vitrifying Hanford Waste, INL/EXT-13-30839*; Idaho National Laboratory: Idaho Falls, ID, 2013.
(35) Boatner, L. A. Synthesis, structure, and properties of monazite, pretulite, and xenotime. *Rev. Mineral. Geochem.* **2002**, *48*, 87−121.
(36) Floran, R.; Abraham, M.; Boatner, L.; Rappaz, M. Geologic stability of monazite and its bearing on the immobilization of actinide wastes. In *Scientific Basis for Nuclear Waste Management*; Moore, J., Ed.; Plenum Press: New York, 1981; Vol. 3, pp 507−514.
(37) Pasteels, P. Uranium-Lead radioactive ages of monazite and zircon from the vire-carolles granite (Normandy). A case of zircon-monazite discrepancy. *Eclogae Geol. Helv.* **1970**, *63*, 231−237.
(38) Bamberger, C.; Haire, R.; Begun, G.; Hellwege, H. The synthesis and characterization of crystalline phosphates of thorium, uranium and neptunium. *J. Less Common Met.* **1984**, *102*, 179−186.
(39) Ewing, R. C.; Wang, L. Phosphates as nuclear waste forms. *Rev. Mineral. Geochem.* **2002**, *48*, 673−699.
(40) Meldrum, A.; Boatner, L.; Ewing, R. Displacive radiation effects in the monazite-and zircon-structure orthophosphates. *Phys. Rev. B* **1997**, *56*, 13805−13814.
(41) Meldrum, A.; Boatner, L. A.; Weber, W. J.; Ewing, R. C. Radiation damage in zircon and monazite. *Geochim. Cosmochim. Acta* **1998**, *62*, 2509−2520.
(42) Oelkers, E. H.; Montel, J.-M. Phosphates and nuclear waste storage. *Elements* **2008**, *4*, 113−116.
(43) Ewing, R. C.; Lutze, W. High-level nuclear waste immobilization with ceramics. *Ceram. Int.* **1991**, *17*, 287−293.
(44) Sales, B.; White, C.; Boatner, L. A comparison of the corrosion characteristics of synthetic monazite and borosilicate glass containing simulated nuclear defense waste. *Nucl. Chem. Waste Manage.* **1983**, *4*, 281−289.
(45) Brow, R. K.; Kim, C. W.; Reis, S. T. Iron polyphosphate glasses for waste immobilization. *Int. J. Appl. Glass Sci.* **2020**, *11*, 4−14.
(46) Day, D.; Wu, Z.; Ray, C.; Hrma, P. Chemically Durable Iron Phosphate Glass Waste forms. *J. Non-Cryst. Solids* **1998**, *241*, 1−12.
(47) Kumar, B.; Lin, S. Redox State of Iron and Its Related Effects in the $CaO-P_2O_5-Fe_2O_3$ Glasses. *J. Am. Ceram. Soc.* **1991**, *74*, 226−228.
(48) Fang, X.; Ray, C. S.; Moguš-Milanković, A.; Day, D. E. Iron redox equilibrium, structure and properties of iron phosphate glasses. *J. Non-Cryst. Solids* **2001**, *283*, 162−172.
(49) Zhoujin, Y.; Tisdale, H. B.; Keerthisinghe, N.; Morrison, G.; Smith, M. D.; Hadermann, J.; Besmann, T. M.; Amoroso, J.; Loye, H.-C. z. A low-temperature, one-step synthesis for monazite can transform monazite into a readily useable advanced nuclear waste form. *Sci. Adv.* **2025**, *11*, No. eadt3518.
(50) Marcial, J.; Chong, S.; Riley, B. J.; Brow, R. K.; Vienna, J. D.; Kim, C. W.; Tang, M. *Bonding Environments and Radiation Stabilities of Phosphate Glasses, PNNL-35754*; Pacific Northwest National Laboratory: Richland, WA, 2024.
(51) Giannuzzi, L. A.; Drown, J. L.; Brown, S. R.; Irwin, R. B.; Stevie, F. A. Applications of the FIB lift-out technique for TEM specimen preparation. *Microsc. Res. Techn.* **1998**, *41*, 285−290.
(52) ASTM C1358-18. *Standard Test Method for Monotonic Compressive Strength Testing of Continuous Fiber-Reinforced Advanced Ceramics with Solid Rectangular Cross Section Test Specimens at Ambient Temperatures*; ASTM International: West Conshohocken, PA, 2018.
(53) ASTM C1220-21. *Standard Test Method for Static Leaching of Monolithic Waste Forms*; ASTM International: West Conshohocken, PA, 2021.
(54) Parruzot, B.; Reiser, J. T.; Lu, X.; Crum, J. V.; Reyes, R. A.; Finucane, K. G.; Witwer, K. S.; Abeta, S.; Yoshioka, M.; Vienna, J. D. Durability evaluation of glasses to immobilize Fukushima (1F) secondary waste using ASTM C1220 (MCC-1) testing. *J. Non-Cryst. Solids X* **2023**, *19*, 100197.
(55) Toby, B. H. R factors in Rietveld analysis: How good is good enough? *Powder Diffr.* **2006**, *21*, 67−70.
(56) Riley, B.; Chong, S.; Emily, N. *Cooling experiments for DPF5-336 reference material made with ERV3b salt simulant, PNNL-33802*; Pacific Northwest National Laboratory, 2023.
(57) Stariha, S. A.; Ebert, W. L. *Durability Assessments of Quenched and Slow-Cooled Iron Phosphate Waste Form Materials, ANL/CFCT-23/24*; Argonne National Laboratory: Lemont, IL, 2023.
(58) Chernyaev, A.; Zhang, J.; Seisko, S.; Louhi-Kultanen, M.; Lundström, M. Fe^{3+} and Al^{3+} removal by phosphate and hydroxide precipitation from synthetic NMC Li-ion battery leach solution. *Sci. Rep.* **2023**, *13*, 21445.
(59) Chong, S.; Riley, B. J. Compositional effects on the chemical durabilities of aluminophosphate glasses: A review. *J. Non-Cryst. Solids X* **2024**, *21*, 100205.
(60) Liu, X.; Qiao, Y.; Qian, Z.; Zhou, S.; Li, L.; Ma, J.; Wang, S.; Qin, Q.; Zhang, Q. Structure and corrosion mechanism of iron phosphate glass with strontium from electrochemical reprocessing. *J. Haz. Mater. Adv.* **2021**, *4*, 100027.
(61) Ray, C. S.; Fang, X.; Karabulut, M.; Marasinghe, G. K.; Day, D. E. Effect of melting temperature and time on iron valence and crystallization of iron phosphate glasses. *J. Non-Cryst. Solids* **1999**, *249*, 1−16.
(62) Wu, Y.; He, W.; Guo, H. Improved fracture toughness and multiple toughening mechanisms of $NdPO_4/NdYbZr_2O_7$ composites. *Ceram. Int.* **2020**, *46*, 16612−16619.
(63) Lee, P.-Y.; Imai, M.; Yano, T. Effects of Sintering Condition on Mechanical Properties of Monazite-Coated Alumina-Fiber/Alumina-Matrix Composites Fabricated by Hot-Pressing. *J. Ceram. Soc. Jpn.* **2004**, *112*, 29−34.
(64) Hikichi, Y.; Ota, T.; Hattori, T. Thermal, mechanical and chemical properties of sintered monazite-(La, Ce, Nd or Sm). *Mineral. J.* **1997**, *19*, 123−130.
(65) Hay, R. S.; Meltzer, P. S.; Marshall, D. B. Monazite Deformation Twinning Research: Research in monazite deformation twinning benefits science and defense, 2006, https://www.mobilityengineeringtech.com/component/content/article/4648-mlh-05-39, accessed June 30, 2025.

https://doi.org/10.1021/acsomega.5c03993
ACS Omega 2025, 10, 33524−33535

(66) Ma, L. N. Dissolution behavior of phosphate glasses, Doctoral Dissertations, Missouri University of Science and Technology, 2014.
(67) Zhu, D.; Kim, C.-W.; Day, D. E. Corrosion behavior of Inconel 690 and 693 in an iron phosphate melt. *J. Nucl. Mater.* **2005**, *336*, 47−53.
(68) Riley, B. J.; Peterson, J. A.; Vienna, J. D.; Ebert, W. L.; Frank, S. M. Dehalogenation of electrochemical processing salt simulants with ammonium phosphates and immobilization of salt cations in an iron phosphate glass waste form. *J. Nucl. Mater.* **2020**, *529*, 151949.

https://doi.org/10.1021/acsomega.5c03993
ACS Omega 2025, 10, 33524−33535